

Seismic observation of tsunami at island broadband stations

Kiwamu Nishida¹, Takuto Maeda², Yoshio Fukao³

¹Earthquake Research Institute, University of Tokyo, 1-1-1 Yayoi 1, Bunkyo-ku, Tokyo 113-0032, Japan

²Hirosaki University, Hirosaki, Japan

³Japan Agency for Marine-Earth Science and Technology, Yokosuka, Japan

Key Points:

- For quantification of seismic observation of tsunami, we evaluate scattering of an incident tsunami for an axisymmetric structure.
- Ground deformation due to the tsunami loading is calculated using static Green's functions.
- By fitting the modeled displacement to observed seismic data, the incident tsunami is inferred from the seismic observation.

Corresponding author: Kiwamu Nishida, knishida@eri.u-tokyo.ac.jp

Abstract

Previous studies have reported seismic observations of tsunami recorded at island broadband stations. Coastal loading by the tsunami can explain them. For further quantification, we model tsunami propagation assuming an axisymmetric structure: a conical island with a flat ocean floor. The total tsunami wavefield can be represented by superposition between an incident tsunami wave and the scattering. The ground deformation due to the total tsunami wavefield at the center is calculated using static Green's functions for elastic half-space with a first-order correction for bathymetry. By fitting the modeled displacement to observed seismic data, we can infer the incident tsunami wave, which can be interpreted as the virtual tsunami amplitude without the conical island. First, we apply this new method to three components of seismic data at a volcano island, Aogashima, for the 2015 Torishima-Oki tsunami earthquake. The estimated tsunami amplitude from the vertical component is consistent with the offshore array observation of absolute pressure gauges close to the island (1.5–20 mHz). The estimated incident azimuth from the three components is also consistent with the offshore array observation. Second, we apply this method to seismic data at four island broadband stations in the Indian ocean for the 2010 Mentawai tsunami earthquake in Indonesia. Despite the limited observed frequency range from 0.5–2.0 mHz, the amplitudes and incident azimuths are consistent with past studies. These observations can complement offshore tsunami observations. Moreover, this method is applicable not only for a tsunami but also for background ocean infragravity wave activity.

1 Introduction

Crustal deformation beneath the ocean due to a massive shallow earthquake generates tsunami (e.g. Satake, 2015). Physically, these are also known as ocean infragravity waves or ocean external gravity waves. Although tsunami amplitudes are usually small in the deep ocean, they increase drastically as tsunami approach the coast. Such large amplitudes cause severe damage in coastal areas. Understanding tsunami propagation is important for effectively evaluating the risk. Tsunami observations are also crucial for characterizing the source processes of an earthquake (e.g. Satake, Fujii, Harada, & Namegaya, 2013). Observations by offshore ocean bottom pressure gauges (*e.g.* Deep-ocean Assessment and Reporting of Tsunamis (DART) (Bernard & Meinig, 2011)) are typically used for source inversion because of simple wave propagation in the pelagic environment.

46 Loading on the seafloor by tsunami causes geodetic deformation of the ground, and
 47 vice versa, which is detectable by land-based broadband seismic stations. For example,
 48 when the 2010 Maule earthquake hit Chile, a high-density tiltmeter network in Japan
 49 recorded ground tilt motions with a typical period of approximately one hour over a broad
 50 inland area facing the Pacific coast (Kimura, Tanaka, & Saito, 2013). Simple 2-D mod-
 51 eling for the deformation induced by the Chilean tsunami explained the observed tilt mo-
 52 tions in the Japanese island arc (Kimura et al., 2013). During the 2004 Sumatra–Andaman
 53 earthquake, tilt motions from 0.3–0.6 mHz were recorded by a broadband seismometer
 54 at Showa station at the mouth of a bay in Antarctica (Nawa et al., 2007), and tilt mo-
 55 tions with typical periods of approximately 1000 s were recorded by broadband seismome-
 56 ters at stations on islands in the Indian ocean (Yuan, Kind, & Pedersen, 2005). Although
 57 the order of observed amplitudes can be explained by tilt motions caused by tsunami load-
 58 ing, the mechanism is not yet fully understood.

59 To quantify ground motions at islands, we model the sloping effects in a semi-analytic
 60 manner for an axisymmetric conical island with a flat ocean floor following Fujima and
 61 Goto (1994). Although the model is simple, it can express the complex wave propaga-
 62 tion close to the shoreline. This simple model can explain the spatial pattern of coastal
 63 tsunami amplification around islands.

64 In section 2, we present the theory of tsunami propagation when an arbitrary tsunami
 65 wavefield enters a conical island following Fujima and Goto (1994). In section 3, we then
 66 estimate the geodetic deformation at the center of the island due to tsunami loading, which
 67 is related to the incident tsunami wavefield. In section 4, using the axisymmetric assump-
 68 tion of single plane wave incidence, we propose a new simple technique for estimating
 69 virtual tsunami amplitude without a conical island, which could be a proxy for offshore
 70 tsunami amplitude. In section 5, this method is applied to two examples: the 2015 Tor-
 71 ishima earthquake in Japan and the 2010 Mentawai tsunami earthquake in Indonesia.

72 **2 Theory of tsunami propagation for a conical island with a flat ocean** 73 **floor**

74 In this study, we consider tsunami scattering around an axisymmetric conical is-
 75 land. For simplicity, we assume that the tsunami can be approximated as a linear long-
 76 wave because dispersion effects should be less important than topographic effects in this
 77 case. Using the long wave approximation, the displacement amplitude of the sea surface

78 disturbance $\eta(r, \theta; \omega)$ satisfies the following governing equation in frequency domain:

$$79 \quad -\omega^2 \eta(r, \theta; \omega) = g_0(h_0 - h(r)) \nabla_h^2 \eta(r, \theta; \omega) + g_0 \nabla(h_0 - h(r)) \cdot \nabla \eta(r, \theta; \omega), \quad (1)$$

80 where r is the radius (Figure 1), g_0 is the gravity constant, ω is the angular frequency,
81 and ∇ represents the spatial gradient in 2-D. The bathymetry $h(r)$ is given by

$$82 \quad h(r) = \begin{cases} h_0 & r < r_0, \\ h_0 - m(r - r_0) & r_0 \leq r < r_1 \\ 0 & r_1 \leq r, \end{cases} \quad (2)$$

83 where r_1 is the radius of the root of the island, r_0 is the radius of the island, h_0 is the
84 sea surface height of the flat ocean from the sea bottom, and m is the slope given by $h_0/(r_1 -$
85 $r_0)$.

86 We note that, for negative frequency, $\eta(r, \theta, -\omega)$ is defined as the complex conjugate
87 by $\eta^*(r, \theta; \omega)$ because the time domain representation should be a real function. A
88 Fourier component at a negative frequency $-\omega$ is, thus, defined by the complex conjugate
89 of that at a positive frequency ω . Here, we use the Fourier convention:

$$90 \quad F(\omega) = \int_{-\infty}^{\infty} f(t) e^{-i\omega t} dt, \quad (3)$$

91 where f is an arbitrary function as a function of time, t , and F is its Fourier component.

92 At high frequency, tsunami velocity $\sqrt{g_0(h_0 - h(r))}$ near the coast decreases to-
93 wards zero because the second term of the right-hand side becomes negligible. The coastal
94 low-velocity region traps tsunami energy, which enhances tsunami run-up height (e.g.
95 Liu, Cho, Briggs, Lu, & Synolakis, 1995; Satake, 2015). Zero velocity at the coast makes
96 the governing equation singular. By using the axisymmetric approximation, however, an
97 analytic evaluation of the singularity becomes possible (Fujima & Goto, 1994).

98 First, let us consider an arbitrary incident arbitrary wavefield $\eta^{in}(r, \theta; \omega)$ in a flat
99 ocean without a conical island virtually. We assume that an arbitrary incident tsunami
100 wave $\eta^{in}(r, \theta; \omega)$ enters the island and is scattered; thus, the total wavefield $\eta(r, \theta; \omega)$ can
101 be represented by superposition between the incident wave and the scattered wave. The
102 wavefield in a flat ocean can be expanded by a Fourier series with respect to the azimuth

103 and Bessel functions of the first kind with respect to the radial direction as follows:

$$\begin{aligned}
 104 \quad \eta^{in}(r, \theta; \omega) &= \frac{1}{2} \zeta_0^{in}(\omega) J_0(k_0 r) \\
 105 \quad &+ \sum_{n=1}^{\infty} [\zeta_n^{in}(\omega) \cos(n\theta) + \zeta_{-n}^{in}(\omega) \sin(n\theta)] J_n(k_0 r), \quad (4) \\
 106
 \end{aligned}$$

107 where J_n is the n th order Bessel function of the first kind, k_0 is the wavenumber given
 108 by $\omega/\sqrt{g_0 h_0}$, and $\zeta_n^{in}(\omega)$ is the coefficient.

109 Because the governing equation is axisymmetric, the total tsunami wavefield $\eta(r, \theta; \omega)$
 110 can also be expanded by a Fourier series with respect to the azimuth as follows:

$$\begin{aligned}
 111 \quad \eta(r, \theta; \omega) &= \frac{1}{2} \phi_0(r; \omega) \\
 112 \quad &+ \sum_{n=1}^{\infty} [\phi_n(\omega) \cos(n\theta) + \phi_{-n}(\omega) \sin(n\theta)], \quad (5) \\
 113
 \end{aligned}$$

114 where $\phi_n(r; \omega)$ is the radial function of azimuthal order n . In the following subsections,
 115 we calculate $\phi_n(r; \omega)$ by evaluating the scattering for an arbitrary incident wave field us-
 116 ing a semi-analytic method (Fujima & Goto, 1994). For the evaluation, we divided the
 117 space into two regions: (I) the flat ocean floor and (II) the sloping bottom of the con-
 118 ical island as shown by Figure 1.

119 2.1 Wave scattering by a conical island in a flat ocean (I)

120 The incident wave $\eta^{in}(r, \theta; \omega)$ enters the conical island area and the scattered wave
 121 amplitude is represented by $\eta^{sc}(r, \theta; \omega)$. The total tsunami amplitude η can be written
 122 as

$$123 \quad \eta(r, \theta; \omega) = \eta^{in}(r, \theta; \omega) + \eta^{sc}(r, \theta; \omega). \quad (6)$$

124 Let us consider the scattered wavefield $\eta^{sc}(r, \theta; \omega)$ for the flat ocean floor (I) (see
 125 Figure 1). The scattered wavefield $\eta^{sc}(r, \theta; \omega)$ can be represented by an outgoing wave
 126 in the flat ocean according to the causality of the scattered wave. For a positive angu-
 127 lar frequency ω , the scattered wavefield can be written as

$$\begin{aligned}
 128 \quad \eta^{sc}(r, \theta; \omega) &= \frac{1}{2} B_0(\omega) \zeta_0^{in}(\omega) H_0^{(2)}(k_0 r) \\
 129 \quad &+ \sum_{n=1}^{\infty} [B_n(\omega) \zeta_n^{in}(\omega) \cos(n\theta) + B_{-n}(\omega) \zeta_{-n}^{in}(\omega) \sin(n\theta)] H_n^{(2)}(k_0 r), \quad (7) \\
 130
 \end{aligned}$$

131 where $H_n^{(2)}(\omega)$ is the n th order Hankel function of the second kind, which represents out-
 132 going waves, and B_n shows the relative amplitudes of the scattered wave.

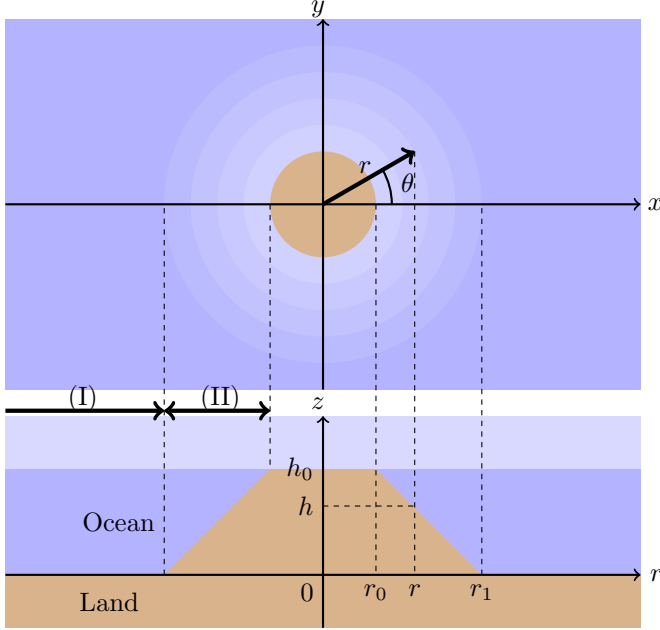


Figure 1. Schematic figure of the conical island. The upper panel shows the plan view of the island, and the lower panel shows the cross-section. The radius on the surface is r_0 and that of the base is r_1 .

133 In summary, $\phi_n(r; \omega)$ (equation 5) in this region (I) is given by

$$134 \quad \phi_n(r; \omega) = \begin{cases} \left(B_n(\omega) H_n^{(2)}(k_0(\omega)r) + J_n(k_0(\omega)r) \right) \zeta_n^{in}(\omega), & n \neq 0, \\ \frac{1}{2} \left(B_0(\omega) H_0^{(2)}(k_0(\omega)r) \right) \zeta_0^{in}(\omega), & n = 0. \end{cases} \quad (8)$$

135 We note that the Bessel functions represent the incident waves and the Hankel functions
136 represent the outgoing scattered waves.

137 2.2 Tsunami wavefield above the sloping bottom in region (II)

138 For the numerical calculation of $\phi_n(r; \omega)$ within region (II) ($r_0 \leq r \leq r_1$), we
139 replace ϕ_n with

$$140 \quad \phi_n(r; \omega) = A_n(\omega) R_n(r; \omega) \zeta_n^{in}(\omega), \quad (9)$$

141 where R_n is normalized to $R_n(r_0; \omega) = 1$ and A_n is the amplitude factor of ϕ_n at $r =$
142 r_0 . Equation 5 in region (II) is rewritten as follows:

$$143 \quad \eta(r, \theta; \omega) = \frac{1}{2} A_0(\omega) \zeta_0^{in}(\omega) R_0(r; \omega) \\ 144 \quad + \sum_{n=1}^{\infty} [A_n(\omega) \zeta_n^{in}(\omega) \cos(n\theta) + A_{-n}(\omega) \zeta_{-n}^{in}(\omega) \sin(n\theta)] R_n(r; \omega). \quad (10)$$

145

146 Inserting $\eta(r, \theta; \omega)$ into the governing equation (equation 1) leads to the following equa-
 147 tion of R_n :

$$148 \frac{d^2 R_n(r; \omega)}{dr^2} + \left(\frac{1}{r} + \frac{1}{h_0 - h(r)} \frac{dh(r)}{dr} \right) \frac{dR(r; \omega)}{dr} + \left(\frac{\omega^2}{g_0(h_0 - h(r))} - \frac{n^2}{r^2} \right) R_n(r; \omega) = 0. \quad (11)$$

149 Following Fujima and Goto (1994), we define the following dimensionless param-
 150 eters, ξ and β , to characterize this system. $\xi(r)$ is the radial phase defined as

$$151 \xi(r) \equiv \int_{r_0}^r k(r') dr' = 2\omega \sqrt{\frac{(h_0 - h(r))}{g_0}}, \quad (12)$$

152 where $k(r)$ is the local wave number given by

$$153 k(r) \equiv \frac{\omega}{\sqrt{g_0(h_0 - h(r))}}. \quad (13)$$

154 β is the azimuthal phase along a circle with a radius of $2r_0$ defined by

$$155 \beta \equiv kr|_{r=2r_0}. \quad (14)$$

156 The reason for choosing this radius is discussed in section 6.

157 The change of variables from r and h to ξ and β leads to the following equation:

$$158 \frac{d^2 R_n(\xi; \omega)}{d\xi^2} + \left(\frac{2\xi}{\xi^2 + \beta^2} + \frac{1}{\xi} \right) \frac{dR_n(\xi; \omega)}{d\xi} + \left(1 - \left(\frac{2\xi}{\xi^2 + \beta^2} \right)^2 n^2 \right) R_n(\xi; \omega) = 0. \quad (15)$$

159 Only in two extreme cases of the radius of the island ($r_0 = 0$ and $r_0 = \infty$) (Fu-
 160 jima & Goto, 1994) can we obtain the analytical solutions of $R(\xi)$, which are crucial for
 161 understanding the behavior of $R(\xi)$. Two independent solutions exist according to the
 162 governing equation; only one satisfies the physical requirement, which is a finite ampli-
 163 tude of η at the shoreline. First, let us consider the analytical solution for an infinite ra-
 164 dius of the island, which also represents a flat sloping bottom. Because β becomes in-
 165 finite, $R_n(0)$ is given by

$$166 R_n(\xi) \sim J_0(\xi). \quad (16)$$

167 Next, let us consider the analytical solution for the zero island radius case $r_0 = 0$. Be-
 168 cause β becomes 0, $R_n(\xi)$ can be given by

$$169 R(\xi) \sim \frac{J_{\sqrt{1+4n^2}}(\xi)}{\xi}. \quad (17)$$

170 Here, we choose a solution that has a finite amplitude at $\xi = 0$. At $\xi = 0$, only $R_0(\xi)$
 171 has a non-zero value, whereas $R_n(0) = 0$ for $n \neq 0$. In general, $R_n(\xi)$ has a signifi-
 172 cant value at $\xi = 0$ when $n \leq \beta$ (Fujima & Goto, 1994). We note that we can nor-
 173 malize all R_n used in this study at $\xi = 0$ because the evaluation of the geodetic defor-
 174 mations requires only R_n for $n = 0, \pm 1$, as discussed in the following sections.

175 This ordinary differential equation can be solved using the numerical Livermore Solver
 176 for Ordinary Differential Equations (LSODE) (Radhakrishnan & Hindmarsh, 1993). Al-
 177 though R_n is integrated from $R_n(0) = 1$ outward with respect to ξ , the governing equa-
 178 tion at $\xi = 0$ is a singularity. For this reason, $R_n(\xi)$ is integrated from $\xi = \Delta\xi$ nu-
 179 merically. $R_n(\Delta\xi)$ can be evaluated analytically by the asymptote (Fujima & Goto, 1994).
 180 $R_n(\Delta\xi)$ can be represented by Taylor expansion up to the second order when $\Delta\xi \ll 1$
 181 and $\beta \neq 0$ (Fujima & Goto, 1994):

$$182 \quad R_n(\Delta\xi) \approx \left(1 - \frac{1}{4}\Delta\xi^2\right). \quad (18)$$

183 Accordingly, the first order initial boundary conditions of R_n at $\xi = \Delta\xi$ are given by

$$184 \quad R_n(\Delta\xi) = 1, \quad (19)$$

$$185 \quad \left.\frac{dR_n(\xi)}{d\xi}\right|_{\xi=\Delta\xi} = -\frac{1}{2}\Delta\xi. \quad (20)$$

187 2.3 Boundary condition between (I) and (II)

188 We evaluate the boundary condition between (I) and (II) at $r = r_1$ for this equa-
 189 tion. Continuity of the amplitude for each azimuthal order, n , and the first derivative
 190 at the boundary between regions (I) and (II) leads to the following boundary condition:

$$191 \quad A_n(\omega)R_n(\xi_1) = J_n(k_0r_1) + B_n(\omega)H_n^{(2)}(k_0r_1), \quad (21)$$

$$192 \quad A_n(\omega) \left(\frac{dR_n(\xi)}{d\xi} \frac{d\xi}{dr} \right) \Big|_{\xi=\xi_1} = \frac{dJ_n(k_0r)}{dr} \Big|_{r=r_1} + B_n(\omega) \frac{dH_n^{(2)}(k_0r)}{dr} \Big|_{r=r_1}, \quad (22)$$

193 where $\xi_1 \equiv \xi(r_1)$. We can estimate A_n and B_n by solving this equation.
 194

195 Figure 2 shows the induced tsunami wavefield with azimuthal order 0 for the unit
 196 amplitude of the incident wave ($\phi_0(r, \omega)/\zeta_0^{in}(\omega)$) at 4 mHz. The parameters are those
 197 for Aogashima given in Table 1. At approximately $r = r_0$, $\phi_0(r; \omega)/\zeta_0^{in}(r; \omega)$ is larger
 198 than 1, which indicates amplification due to confinement along the coast. We discuss this
 199 in detail in section 6.

200 3 Geodetic deformation by tsunami loading

201 To estimate ground motions due to tsunami, we assume that they can be repre-
 202 sented by static deformation caused by tsunami loading (e.g. Sorrells & Goforth, 1973)
 203 because the phase velocity of seismic waves (on the order of 4 km/s) is much faster than
 204 that of a tsunami (on the order of 0.01 km/s) in coastal areas. Loading on the seafloor

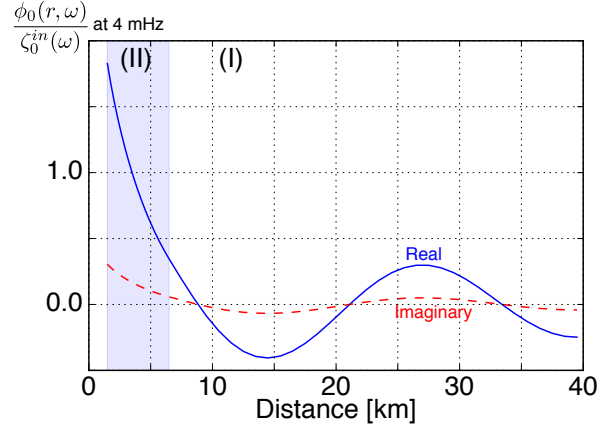


Figure 2. $\phi_0(r; \omega)/\zeta_0(\omega)$ at 4 mHz for Aogashima, the parameters of which are given in Table 1. The blue line shows the real part and the red dashed line shows the imaginary part.

Table 1. Parameters (radius of the island r_0 , slope m , and ocean depth h_0) used in this study based on ETOPO1 (Amante & Eakins, 2009). These parameters were estimated by the non-linear least-squares technique using MINPACK (Moré et al., 1984) with trial and error. f_β is a reference frequency used as $\beta = 1$ in equation 14.

station	radius r_0 [km]	slope m	ocean depth h_0 [km]	f_β [mHz]
AOG	1.5	0.20	1.0	2.9
RER	29	0.070	4.2	0.39
AIS	4.9	0.18	2.0	1.5
DGAR	12	0.017	4.2	0.29
CRZF	10	0.034	3.0	0.45

205 by the modeled tsunami wavefield is convolved with static Green’s functions in a semi-
 206 infinite medium with the following correction for bathymetric effects. Because the ra-
 207 dius of the island, r_0 , is much smaller than r_1 in most cases, we evaluate the deforma-
 208 tion, $\mathbf{u}(\omega)$, at the center of the island for simplicity. Note that the tilt motion at the cen-
 209 ter is also calculated because the horizontal component of a broadband seismometer is
 210 sensitive to tilt motion (Aki & Richards, 1980).

211 To evaluate the bathymetric correction for the Green’s functions in a semi-infinite
 212 medium, the displacement $\mathbf{u}(x, y, z)$ and stress $\boldsymbol{\sigma}(x, y, z)$ in a Cartesian coordinate sys-
 213 tem (x, y, z) is expanded by the powers of slope, m , up to the first order (Segall, 2010;

214 Williams & Wadge, 2000):

$$215 \quad u_i(x, y, z; \omega) = u_i^{(0)}(x, y, z; \omega) + u_i^{(1)}(x, y, z; \omega)m + \mathcal{O}(m^2), \quad i = x, y, z \quad (23)$$

$$216 \quad \sigma_{ij}(x, y; \omega) = \sigma_{ij}^{(0)}(x, y, z; \omega) + \sigma_{ij}^{(1)}(x, y, z; \omega)m + \mathcal{O}(m^2), \quad i, j = x, y, z, \quad (24)$$

218 where \mathcal{O} indicates "order of", u_i is the displacement, σ_{ij} is the stress, $^{(0)}$ shows the 0th
 219 order term, and $^{(1)}$ shows the first order terms. Based on the estimation of the first or-
 220 der terms described in appendix A, the first order terms with respect to the slope, m ,
 221 becomes comparable to the second order terms. Therefore, we neglect the first order terms
 222 below.

223 The displacement and tilt on the surface ($z = h_0$) and at the center ($x = y =$
 224 0) are corrected for elevation from $z = 0$ as follows:

$$225 \quad u_k(0, 0, h_0) = u_k^{(0)}(0, 0, 0) - h_0 \left. \frac{\partial u_z^{(0)}}{\partial x_k} \right|_{z=0}, \quad k = x, y, \quad (25)$$

$$226 \quad u_z(0, 0, h_0) = u_z^{(0)}(0, 0, 0), \quad (26)$$

$$227 \quad \left. \frac{\partial u_z}{\partial x_k} \right|_{x=y=0, z=h_0} = \left. \frac{\partial u_z^{(0)}}{\partial x_k} \right|_{x=y=z=0}, \quad k = x, y. \quad (27)$$

229 The first-order corrections of horizontal displacement according to the location change
 230 are related to the corresponding 0th-order tilt motions. The correction of vertical dis-
 231 placement and tilt motion according to the location change is negligible in the first or-
 232 der because the surface pressure causes a vertical strain $\partial u_z^{(0)}/\partial z = 0$ at the free sur-
 233 face in a half space (Farrell, 1972).

234 Static Green's functions $g_r^z(r)$, $g_\theta^z(r)$, and $g_z^z(r)$ at a surface point $\mathbf{r} = (r, \theta, 0)$ for
 235 a vertical force at the origin in a semi-infinite medium are given by (Jaeger, Cook, & Zim-
 236 merman, 2007; Segall, 2010)

$$237 \quad g_r^z(r) = \frac{1}{4\pi} \frac{1}{\lambda + \mu} \frac{1}{r}, \quad (28)$$

$$238 \quad g_\theta^z(r) = 0, \quad (29)$$

$$239 \quad g_z^z(r) = \frac{1}{4\pi\mu} \frac{\lambda + 2\mu}{\lambda + \mu} \frac{1}{r}, \quad (30)$$

241 where r is the radius in a cylindrical coordinate system (Figure 1), μ , and λ are Lamé's
 242 constant of the ground, the superscript on the Green's tensors refers to the direction of
 243 the point force, and the subscript refers to the direction of displacement. By convolv-
 244 ing forcing by the total tsunami wavefield and the static Green's functions with bathy-
 245 metric corrections, we can estimate the displacement and tilt at the center.

4 Virtual tsunami amplitude and direction without a conical island

Based on the total tsunami wavefield (section 2) and the Green's functions (section 3), we can relate the ground particle velocity at the center to the incident tsunami using a transfer function. The symmetric assumption of the island simplifies the transfer function concerning the azimuthal dependence. By deconvolving the transfer function from observed seismic data in the vertical component, we can infer the incident tsunami amplitude, η^v , at the center assuming that the island is virtually removed. By deconvolving the transfer function from observed seismic data in the horizontal component, we can estimate the spatial gradient of η^v , which shows the propagation direction together with a single plane wave assumption.

4.1 Transfer function of the vertical component

The vertical ground velocity at the origin $v_z(\omega)$ due to tsunami deformation can be represented by convolution between tsunami loading and the static Green's function as:

$$v_z(\omega) = -\rho g_0 \omega e^{\pi i/2} \int_{r_0}^{\infty} \int_0^{2\pi} \eta(r, \theta; \omega) g_z^z(r) r dr d\theta, \quad (31)$$

where $v_z(\omega)$ is the particle velocity in the z component given by $i\omega u_z(\omega)$. Because we consider vertical deformation at the center of the island, the higher order contributions ($n \geq 1$) are canceled out. Here, we define the virtual tsunami amplitude, $\eta^v(\omega)$, without the island as

$$\eta^v(\omega) \equiv \eta^{in}(r, \theta; \omega)|_{r=0}. \quad (32)$$

The virtual tsunami amplitude can be related to the particle velocity v_z using a transfer function $T_{\eta z}$:

$$v_z(\omega) = T_{\eta z}(\omega) \eta^v(\omega), \quad (33)$$

where $T_{\eta z}(\omega)$ is the transfer function of the tsunami to vertical ground velocity, defined as

$$T_{\eta z}(\omega) \equiv -e^{\pi i/2} \pi \omega \rho g_0 (I_1^z(\omega) + I_2^z(\omega)), \quad (34)$$

The integrals I_1^z and I_2^z are defined as

$$I_1^z(\omega) \equiv \int_{r_1}^{\infty} \left(B_0(\omega) H_0^{(2)}(k_0 r) + J_0(k_0 r) \right) g_z^z(r) r dr, \quad (35)$$

$$I_2^z(\omega) \equiv \int_{r_0}^{r_1} A_0(\omega) R_0(r) g_z^z(r) r dr, \quad (36)$$

276 respectively. Figure 3a shows an example of the vertical transfer function $T_{\eta z}(\omega)$ for Ao-
 277 gashima. Below 5 mHz, the transfer function is flat. At 0 frequency, the amplitude and
 278 phase of the transfer function can be explained by the theoretical solution for a flat ocean
 279 (Ben-Menahem & Singh, 2000) as discussed in section 6. The amplitude decreases with
 280 frequency above 5 mHz because tsunami wavelength becomes smaller than the island scale
 281 r_0 .

4.2 Transfer function of the horizontal component

282
 283 Let us consider the transfer function of the horizontal component for tsunami inci-
 284 dence in the same manner. The horizontal ground velocity at the origin $\mathbf{v}_h(\omega)$ due to
 285 tsunami deformation can be represented by

$$\mathbf{v}_h(\omega) \equiv \begin{pmatrix} v_x(\omega) \\ v_y(\omega) \end{pmatrix} = -\rho g_0 \omega e^{\pi i/2} \int_{r_0}^{\infty} \int_0^{2\pi} \eta(r, \theta; \omega) \left(g_r^z - h_0 \frac{\partial g_z^z}{\partial r} \right) \begin{pmatrix} -\cos \theta \\ -\sin \theta \end{pmatrix} r dr d\theta. \quad (37)$$

287 Because we consider the horizontal displacement at the center of the island, only $n \pm$
 288 1 in terms of η contributes to the integration, as follows:

$$\begin{pmatrix} v_x(\omega) \\ v_y(\omega) \end{pmatrix} = \frac{i}{2} T_{\eta h}(\omega) \begin{pmatrix} \zeta_1^{in} \\ \zeta_{-1}^{in} \end{pmatrix} = i \frac{T_{\eta h}(\omega)}{k_0} \nabla \eta^{in}(r, \theta; \omega)|_{r=0}. \quad (38)$$

290 Here, $T_{\eta h}(\omega)$ is given by,

$$T_{\eta h}(\omega) = 2\pi\omega\rho g_0 (I_1^h(\omega) + I_2^h(\omega)), \quad (39)$$

292 where integrals I_1^h and I_2^h are defined as

$$I_1^h(\omega) \equiv \int_{r_1}^{\infty} \left(B_1(\omega) H_1^{(2)}(k_1 r) + J_1(k_1 r) \right) \left(g_r^z - h_0 \frac{\partial g_z^z}{\partial r} \right) r dr, \quad (40)$$

$$I_2^h(\omega) \equiv \int_{r_0}^{r_1} A_1(\omega) R_1(r) g_r^z(r) r dr. \quad (41)$$

296 The spatial gradient of the surface displacement $\nabla \eta|_{r=0}$ can be related to the flow rate,
 297 \mathbf{Q} (Satake, 2015), at the origin defined as

$$\mathbf{Q} = \int_0^h \mathbf{v}_h dz = \frac{i g_0}{\omega} \nabla \eta^{in}|_{r=0} \quad (42)$$

299 For simplicity, we assume that η can be represented by a single plane wave inci-
 300 dence with the relative travel time, $\mathcal{T}(r, \theta)$, to the origin. The gradient can be written
 301 as

$$\nabla \eta^{in}(r, \theta; \omega) = -i\omega \eta^{in}(0, \theta; \omega) \nabla \mathcal{T}(r, \theta) = \eta^{in}(0, \theta; \omega) (-ik_0) \mathbf{e}_r, \quad (43)$$

303 where \mathbf{e}_r is the propagation direction of the tsunami. Then, we obtain the following re-
 304 lationship:

$$305 \quad \mathbf{v}_h(\omega) = T_{\eta h}(\omega)\eta^v(\omega)\mathbf{e}_r. \quad (44)$$

306 $T_{\eta h}$ represents the transfer function from the tsunami incidence to horizontal ground ve-
 307 locity at the center. This result shows that the observed ground velocity is parallel to
 308 the tsunami propagation direction under these simple assumptions. Figure 3a shows an
 309 example of the horizontal transfer function $T_{\eta z}(\omega)$ for Aogashima. The transfer func-
 310 tion has a broad peak at 5 mHz. At 0 frequency, the amplitude and phase of the trans-
 311 fer function can be explained by the theoretical solution for a flat ocean (Ben-Menahem
 312 & Singh, 2000) as discussed in section 6. The amplitude also decreases with frequency
 313 above 5 mHz.

314 Below 1 mHz, tilt motion induced by tsunami is dominant in the horizontal com-
 315 ponent of seismic sensors (Kimura et al., 2013; Nawa et al., 2007). The horizontal ac-
 316 celeration contribution due to tilt motion (∇u_z , where u_z is the vertical displacement)
 317 is given by $g_0\nabla u_z$ (e.g. Rodgers, 1968; Wielandt & Forbriger, 1999). Then, the tilt mo-
 318 tion at the origin, $v(\omega)$, due to deformation by the tsunami can be represented by

$$319 \quad \mathbf{v}_h^{tilt}(\omega) = \frac{g_0\nabla u_z}{i\omega} = \frac{-\rho g_0}{i\omega} \int_{r_0}^{\infty} \int_0^{2\pi} \eta(r, \theta; \omega) \frac{\partial g_r^z}{\partial r} \begin{pmatrix} -\cos\theta \\ -\sin\theta \end{pmatrix} r dr d\theta. \quad (45)$$

320 The higher order contributions ($n \neq \pm 1$) are again canceled out.

$$321 \quad \mathbf{v}_h^{tilt}(\omega) = \frac{i}{2} T_{\eta h}(\omega) \begin{pmatrix} \zeta_1^{in} \\ \zeta_{-1}^{in} \end{pmatrix} = i \frac{T_{\eta h}^{tilt}(\omega)}{k_0} \nabla \eta^{in}(r, \theta; \omega)|_{r=0}. \quad (46)$$

322 Here, the transfer function due to tilt, $T_{\eta h}^{tilt}(\omega)$, of the tsunami to horizontal ground ve-
 323 locity is given by,

$$324 \quad T_{\eta h}^{tilt}(\omega) = \frac{2\pi\rho g_0}{\omega} (I_1^t(\omega) + I_2^t(\omega)), \quad (47)$$

325 where integrals I_1^t and I_2^t are defined by

$$326 \quad I_1^t(\omega) \equiv \int_{r_1}^{\infty} \left(B_1(\omega) H_1^{(2)}(k_1 r) + J_1(k_1 r) \right) \frac{\partial g_h^r(r)}{\partial r} r dr, \quad (48)$$

$$327 \quad I_2^t(\omega) \equiv \int_{r_0}^{r_1} A_1(\omega) R_1(r) \frac{\partial g_z^z(r)}{\partial r} r dr. \quad (49)$$

328
 329 Then, we also obtain the following relationship:

$$330 \quad \mathbf{v}_h^{tilt}(\omega) = T_{\eta h}^{tilt}(\omega)\eta^v(\omega)\mathbf{e}_r. \quad (50)$$

Figure 3b shows that the tilt effects of the horizontal transfer function are dominant, specifically at low frequencies. Below 1 mHz, the transfer function approaches the theoretical solution for a flat ocean (Ben-Menahem & Singh, 2000), which is proportional to ω^{-1} . With increasing frequency, the contribution of the tilt effect decreases. Although the amplitudes of horizontal components are an order of magnitude larger than those of vertical components, the estimated virtual tsunami amplitude from horizontal components is more ambiguous. This is because tilt motions, which are the spatial derivative of vertical motion, are more sensitive to small-scale bathymetric changes and crustal heterogeneity.

5 Comparison with observations

During huge shallow earthquakes, the horizontal components of broadband seismometers located on an island often record tilt motion associated with tsunami (e.g., the 2004 Sumatra earthquake (Yuan et al., 2005)), although the contribution of low-frequency seismic waves excited by the earthquake (Kimura et al., 2013; Yuan et al., 2005) disturbs the tsunami signal. The amplitudes of vertical components are too small to detect because the vertical response is much smaller than the tilt response, as shown in Figure 3.

In order to suppress the noise, we apply this method to tsunami earthquakes, which cause a much larger tsunami than expected from the seismic moment. We determine the virtual tsunami amplitude and direction for two tsunami earthquakes: (1) the 2015 volcanic tsunami earthquake near Torishima, Japan, and (2) the 2010 Mentawai tsunami earthquake in Indonesia. These results are verified by ray theory and other geophysical observations.

5.1 Torishima 2015 Earthquake in Japan

A compensated-linear-vector-dipole (CLVD) type earthquake occurred on May 2, 2015, near Torishima island, Izu–Bonin arc, Japan (Figure 4), generating an abnormally large tsunami (e.g. 0.5 m at Hachijozima 180 km north of the epicenter) for the moment magnitude of M_w 5.7, determined by the U.S. Geological Survey. The tsunami was caused by large deformation in a shallow part of a submarine volcanic body (Fukao et al., 2018). A triangular array of ocean bottom pressure (OBP) gauges recorded an off-shore tsunami

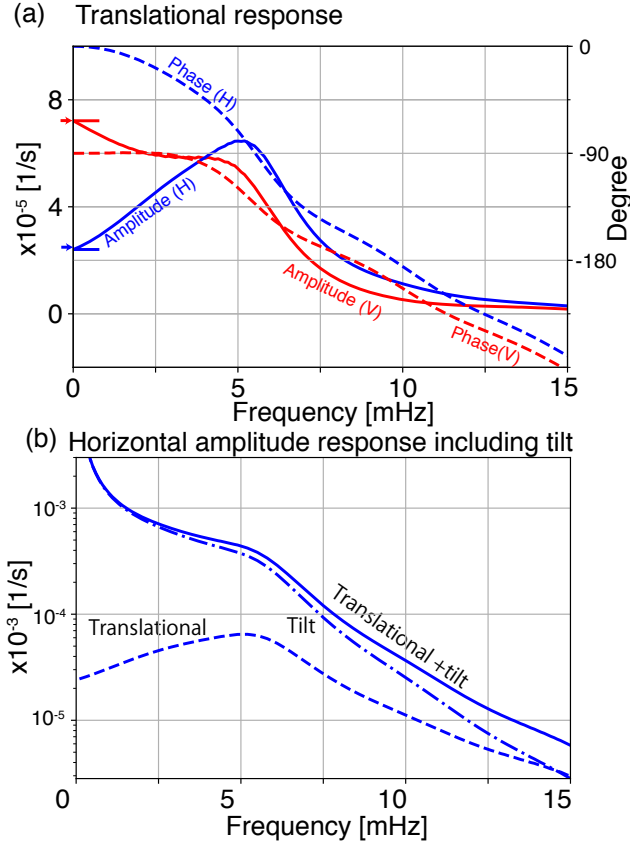


Figure 3. (a) Transfer function of translational motions against frequency. The dashed lines show the amplitudes and the solid lines shows the phase, where (V) in the figure represents the vertical component and (H) shows the horizontal component. The red and blue lines show the vertical and horizontal transfer functions, respectively. Red and blue arrows at 0 mHz show the theoretical amplitudes for a flat ocean (Ben-Menahem & Singh, 2000) in vertical and horizontal components respectively. The phase shift can be explained by the arrival delay (approximately 70 s). (b) Amplitude of the transfer function of the horizontal component against frequency according to the contribution of translational motion, tilt motion, and both. The contribution of tilt motion is dominant below 5 mHz. We note that the phases of these contributions are the same at all frequencies.

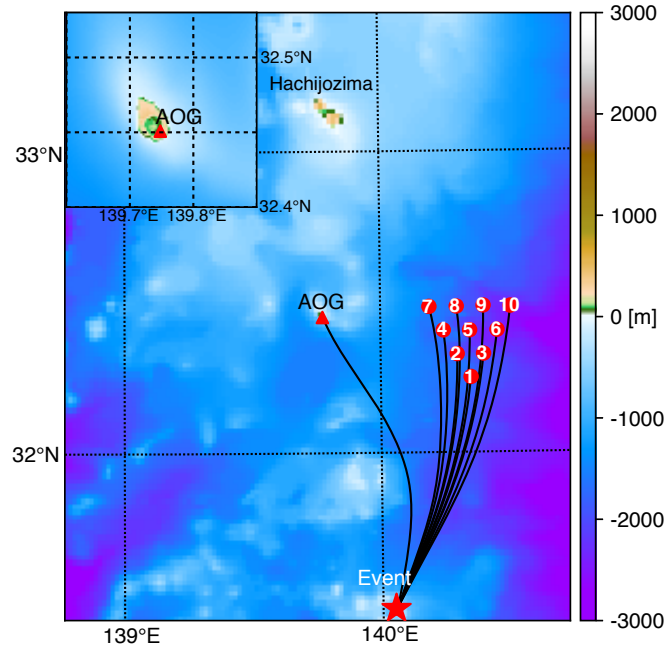


Figure 4. Station distribution of an array of 10 offshore pressure gauges (triangles). The inset shows an enlarged map of Aogashima (AOG). The star symbol shows the hypocenter of the earthquake near Torishima on May 2, 2015. At approximately 33.1°N , Hachijojima north to Aogashima is also shown. The station numbers are shown in red circles.

361 (Sandambata et al., 2017). They were deployed 100 km northeast of the epicenter with
 362 a station separation of approximately 10 km (Figure 4). All tsunami waveforms with am-
 363 plitudes of approximately 2 cm are similar to each other (Figure 5). A tsunami earth-
 364 quake with a surface wave magnitude of M_s 5.6 in the same area occurred on June 13,
 365 1984 (Kanamori, Ekström, Dziewonski, Barker, & Sipkin, 1993; Satake & Kanamori, 1991);
 366 their focal mechanisms suggest magma injection with the submarine volcano (Fukao et
 367 al., 2018; Kanamori et al., 1993).

368 At Aogashima island, close to the array, a broadband seismometer (STS2) of F-
 369 net (Okada et al., 2004) was deployed by the National Research Institute for Earth Sci-
 370 ence and Disaster Prevention (NIED). Because seismic waves from tsunami earthquakes
 371 were relatively small at a low-frequency of 1.5-20 mHz, the broadband seismometer recorded
 372 clear ground motions associated with the tsunami. We can compare the estimated vir-
 373 tual tsunami amplitudes from the seismic observations with near deep ocean bottom pres-
 374 sure gauge.

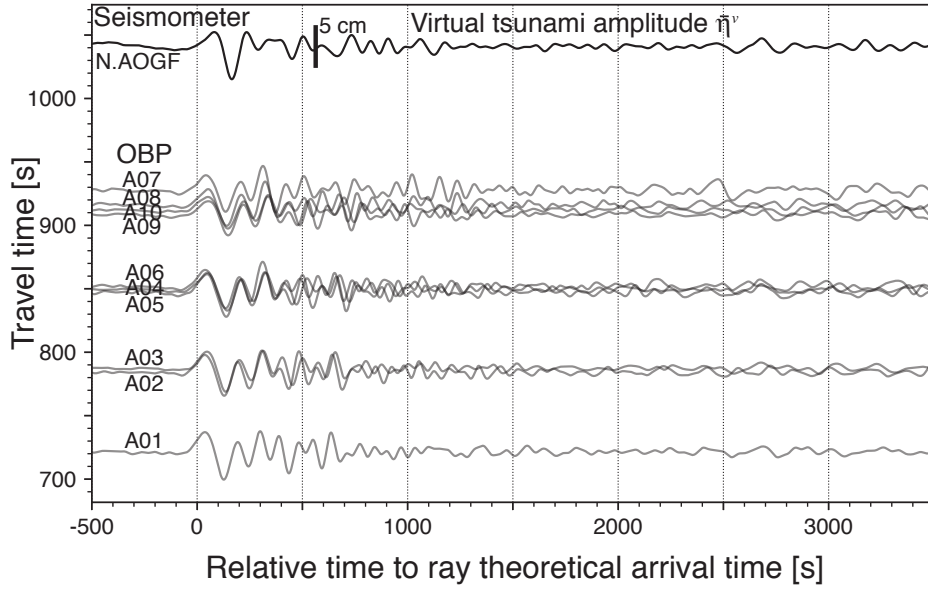


Figure 5. Estimated virtual tsunami amplitude with array observations by absolute pressure gauges. The vertical axis shows travel time predicted by ray theory and the horizontal axis shows relative time to the ray theoretical arrival time. Here, travel times are calculated by fast marching (Rawlinson, 2005; Rawlinson & Sambridge, 2005) using the long wave approximation. The uppermost record shows the virtual tsunami amplitude estimated from the vertical ground velocity at Aogashima (N.AOGF). The lower record shows 10 records of ocean bottom pressure gauges. These records are bandpass filtered from 1.5 to 20 mHz (4th order Butterworth, zero phase). The amplitude scales are the same throughout all records. The maximum amplitudes are approximately 2 cm.

375 Using the vertical component of the broadband seismometer, we infer the virtual
 376 tsunami amplitude. The modeled parameters of the conical island are given in Table (1).
 377 Using the transfer function, $T_{\eta z}(\omega)$, shown by Figure 3a, we estimate the virtual tsunami
 378 amplitude $\bar{\eta}^v(\omega)$ by deconvolution:

$$379 \quad \bar{\eta}^v(\omega) = \frac{T_{\eta z}^*(\omega)}{T_{\eta z}^*(\omega)T_{\eta z}(\omega) + w} v_z(\omega), \quad (51)$$

380 where w is the water level, which is 5×10^{-3} of the squared amplitude of $T_{\eta z}$ at 5 mHz.
 381 The $\bar{\eta}^v$ is converted in time domain. Figure 5 shows the comparison of $\bar{\eta}^v(t)$ with ob-
 382 served tsunami amplitudes by the pressure gauges against the relative travel time. The
 383 estimated amplitude of approximately 2.5 cm and the relative travel times are consis-
 384 tent with the offshore observations. The ray theoretical arrival times should coincide with

385 the peak time but the figure shows slight delays in the peak time, which are attributed
 386 to dispersion due to the finite wavelength. This result verifies the feasibility of this method.

387 Next, let us consider the propagation direction from the observed horizontal com-
 388 ponents shown in Figure 3b. Using the transfer function, $T_{\eta h}$, for horizontal components,
 389 the tsunami amplitude with a propagation direction of $(\bar{\eta}_x^v, \bar{\eta}_y^v)$ can be defined as,

$$390 \begin{pmatrix} \bar{\eta}_x^v(\omega) \\ \bar{\eta}_y^v(\omega) \end{pmatrix} \equiv \frac{T_{\eta h}^*}{T_{\eta h}^*(\omega)T_{\eta h}(\omega) + w} \begin{pmatrix} v_x(\omega) \\ v_y(\omega) \end{pmatrix}, \quad (52)$$

391 where w is the water level, which is 1×10^{-3} the squared amplitude of $T_{\eta h}$ at 5 mHz.
 392 With the single plane wave assumption, $(\bar{\eta}_x^v, \bar{\eta}_y^v)$ can be interpreted as $\eta^{in} \mathbf{e}_r$ (equation
 393 44). Figure 6a shows the comparison among $\bar{\eta}_x^v$, $\bar{\eta}_y^v$, and $\bar{\eta}^v$. The waveforms at approx-
 394 imately 1000 s are consistent with each other.

395 The particle motions of the horizontal components shown in Figure 6b shows a lin-
 396 ear polarization, which is consistent with the ray path shown in Figure 4. The consis-
 397 tency suggests that the assumptions related to the approximations of the conical island
 398 and the single plane wave are appropriate. Although the horizontal amplitude is slightly
 399 larger than the vertical amplitude, the discrepancy can be attributed to the slightly off-
 400 center station to the southwest. Phases of the later arrival at approximately 3000 s in
 401 Figure 6 are different in different components because they are composed of multiple scat-
 402 tering waves.

403 To quantitatively estimate the propagation direction, we assume that the virtual
 404 tsunami amplitude is given by $\bar{\eta}^v$ from the vertical component. Then, equation 44 leads
 405 to

$$406 \begin{pmatrix} \bar{\eta}_x^v(\omega) \\ \bar{\eta}_y^v(\omega) \end{pmatrix} = \bar{\eta}^v \begin{pmatrix} \sin \varphi \\ \cos \varphi \end{pmatrix}, \quad (53)$$

407 where φ is the propagation azimuth, which, in this case, can be estimated by

$$408 \varphi = \frac{\pi}{2} - \arctan \left(\frac{\int \bar{\eta}_y^v(t) \bar{\eta}^v(t) dt}{\int \bar{\eta}_x^v(t) \bar{\eta}^v(t) dt} \right) \quad (54)$$

409 The red arrow in Figure 6 shows the propagation direction φ , whose length shows the
 410 root mean squared amplitude from 0 to 5000 s. Because the cross-correlation procedure
 411 suppresses incoherent parts, which originate from the higher noise level and scattered
 412 wavefield, the estimation is expected to be robust. Figure 7 shows the comparison be-
 413 tween the estimated azimuth and the ray azimuth at the station. This figure shows that
 414 they are consistent within 10 degrees.

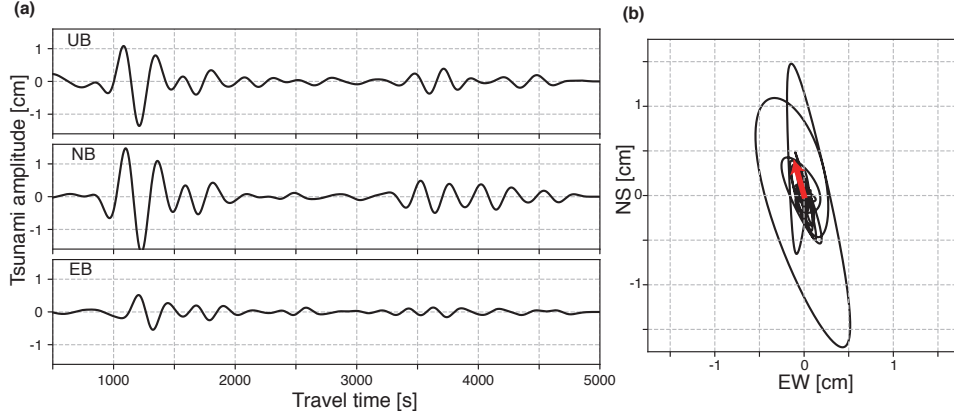


Figure 6. (a) The three components of the estimated tsunami waveform. The first is 2–5 mHz with a 6th order Butterworth filter. (b) Particle motions of the horizontal components from 2 to 5 mHz. The red arrow shows the estimated propagation direction with root mean squared amplitudes from 0 to 500 s.

415 5.2 Mentawai 2010 in Indonesia

416 The 2010 Mentawai earthquake (Mw 7.8) caused a destructive tsunami in the Mentawai
 417 Islands, west of Sumatra in Indonesia (Satake, Nishimura, et al., 2013). The tsunami am-
 418 plitude reached 9.3 m on the west coasts of North and South Pagai Island. Seismolog-
 419 ical data analyses show that the earthquake was a tsunami earthquake (e.g. Lay et al.,
 420 2011). For the analysis, we use four broadband stations located on islands DGAR, RER,
 421 CRZF, and AIS shown in Figure 8. For the estimation of tsunami amplitude, we use the
 422 water level, which is 5% of the maximum squared amplitude.

423 Because most island radii (Table 1) are larger than that of Aogashim, as shown in
 424 Figure 9, their transfer functions are not sensitive to tsunami above 1 mHz. Hence, we
 425 focus on a signal with a typical frequency of 1 mHz, as shown in Figure 10. The esti-
 426 mated virtual tsunami amplitudes were 0.4 cm at DGAR, 1.3 cm at AIS, 0.9 cm at CRZF,
 427 and 0.6 cm at RER. Arrival times of the estimated waveforms are consistent with the
 428 ray theoretical values. The arrival time at DGAR is advanced because the simple sym-
 429 metric model is too simple to model a large island with a larger root size r_1 of approx-
 430 imately 260 km (see Table 1). Although DART station 5601 recorded a maximum tsunami
 431 amplitude of 1 cm (Satake, Nishimura, et al., 2013), it is located 1,600 km south to the
 432 epicenter. Because there are no offshore stations close to the four seismic broadband sta-

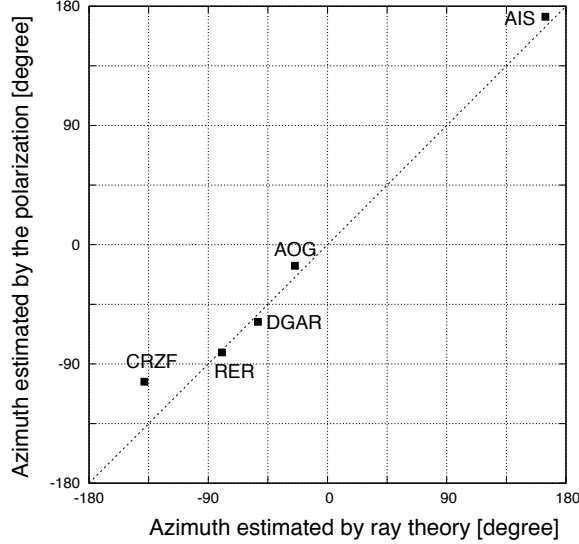


Figure 7. Propagation azimuths at stations. The horizontal axis shows the propagation azimuths estimated by this method utilizing broadband seismic data, whereas the vertical axis shows azimuths based on ray theory.

433 tions, we compare the virtual tsunami heights $\bar{\eta}^v$ with a numerical results by NOAA cen-
 434 ter for Tsunami Research, which are maximum tsunami heights at an offshore points close
 435 to the stations based on the NOAA forecast method using MOST model with the tsunami
 436 source inferred from DART data (Gica, Spillane, Titov, Chamberlin, & Newman, 2008).
 437 The calculated maximum wave heights of about 5 mm for RER, about 14 mm for AIS,
 438 about 14 mm, and about 8 mm for CRZF are consistent with our estimations.

439 The map in Figure 8 shows the estimated propagation directions using three com-
 440 ponents of broadband seismometers, as shown in the previous subsection. Although the
 441 estimated azimuths are slightly different from the ray paths on this large scale, the dif-
 442 ference can be attributed to strong refraction close to the islands. Indeed, the relation-
 443 ship between the propagation azimuths estimated from the seismic stations can be ex-
 444 plained by the azimuths predicted by ray theory, as shown in Figure 7. These are con-
 445 sistent with ray paths within 10 degrees except for CRZF. The deviation could be ex-
 446 plained by scattering due to the neighboring island shown in Figure 9, which may break
 447 the single plane wave approximation.

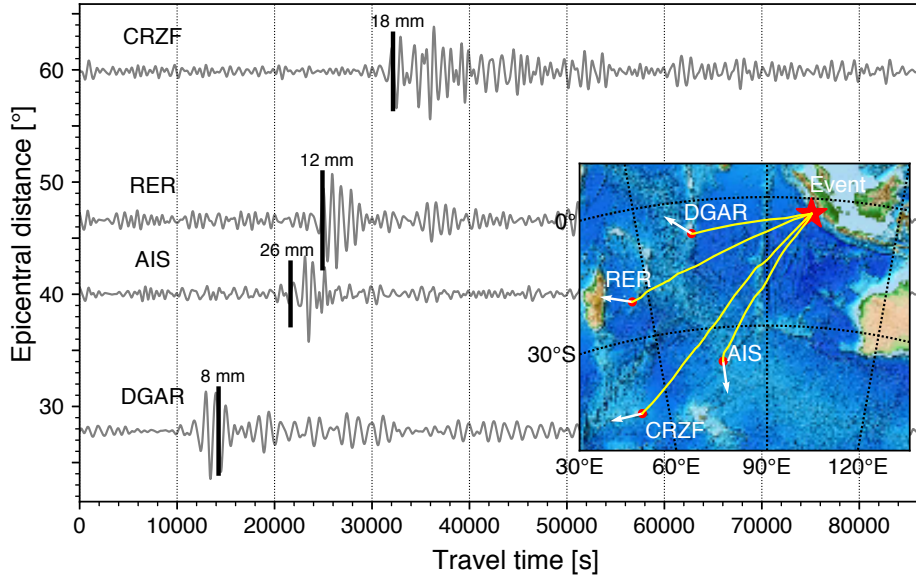


Figure 8. Virtual tsunami amplitudes at four stations for the 2010 Mentawai earthquake (Oct 25, 2010). 0.7–2 mHz (order 6). The map in the inset shows the station locations and the earthquake location. The bold black bars show the corresponding ray theoretical arrival times with amplitude scales.

6 Characteristics of the transfer function according to the slope and radius

Tsunami trapping in the coastal slope of a conical island is crucial for characterizing the transfer functions. This section describes the amplification characteristics due to trapping in coastal areas, where the trapping condition (Longuet-Higgins, 1967) is given by,

$$\frac{\partial}{\partial r} \left(\frac{h(r)}{r^2} \right) \geq 0. \quad (55)$$

For the case of a conical island, the condition can be simplified as

$$r \leq 2r_0. \quad (56)$$

This relationship indicates that a larger conical island will trap more inshore areas.

β defined in equation 14 is crucial for characterizing the trapping effect. β can be interpreted as the ratio of the circumference, $4\pi r_0$ at $r = 2r_0$, to the wavelength, λ . In other words, β shows the azimuthal number of nodes of the trapping mode. Here, we define the cut-off frequency f_β as $\beta = 1$. Above this frequency, the tsunami is trapped

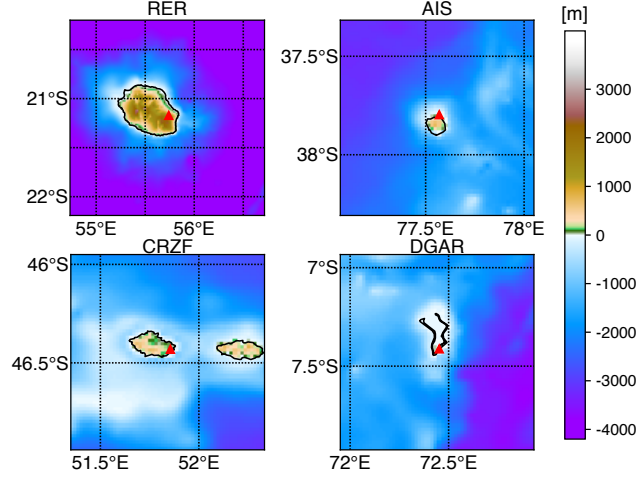


Figure 9. Enlarged maps of the islands. Stations are indicated by red triangles.

462 in inshore areas. f_β is also a good proxy for geodetic deformation at the center because
 463 the deformation becomes significant when the radius of the island becomes larger than
 464 the wavelength. Consequently, the geodetic deformation becomes small with increasing
 465 frequency above the frequency. The f_β value therefore characterizes the cut-off frequency
 466 of the transfer functions. Table 1 shows f_β for the islands, which correspond to the cut-
 467 off frequency shown in Figure 10.

468 With a smaller slope m , more tsunami energy is trapped in the inshore area due
 469 to the slow propagation speed. In this case, the transfer function exhibits a peak at ap-
 470 proximately f_β . The translational transfer functions of DGAR and CRZF with smaller
 471 slope, m , show peaks at approximately f_β . Thus, f_β could be a proxy for the charac-
 472 teristics when evaluating the transfer function,.

473 At much lower frequencies than f_β , we can neglect scattering by the island because
 474 the wavelength of the tsunami becomes much larger than the island scale. Moreover, the
 475 contribution of geodetic deformation in the inshore area becomes negligible. In this limit,
 476 the transfer functions are approximated by those of a semi-infinite medium loaded by
 477 pressure fluctuations on the surface given by Ben-Menahem and Singh (2000):

$$478 \quad \lim_{\omega \rightarrow 0} T_{\eta z}(\omega) = \frac{e^{-\pi i/2} \sqrt{g_0 h} \lambda + 2\mu}{2(\lambda + \mu)} \frac{\lambda + 2\mu}{\mu} \rho g_0, \quad (57)$$

$$479 \quad \lim_{\omega \rightarrow 0} T_{\eta h}(\omega) = \frac{\sqrt{g_0 h}}{2(\lambda + \mu)} \rho g_0. \quad (58)$$

480

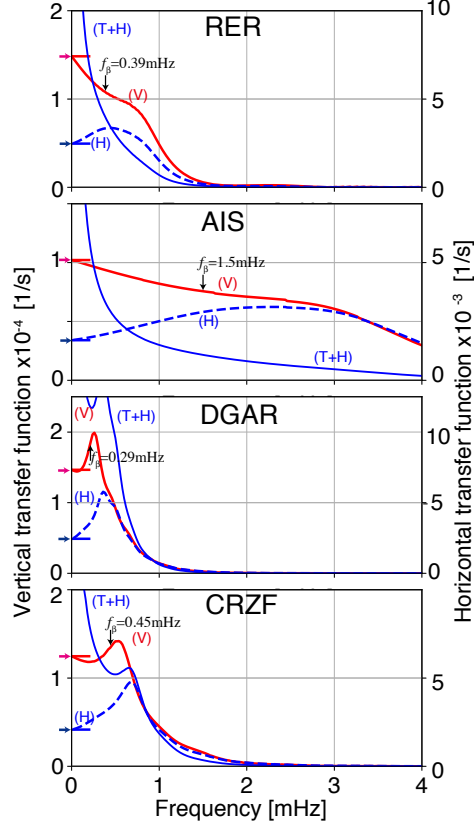


Figure 10. Amplitudes of transfer functions for vertical components shown by solid red lines and horizontal components shown by blue dashed lines against frequency at the four broadband stations, composed of one IRIS IDA station, DGAR (Diego Garcia, Chagos islands), and three GEOSCOPE stations RER (La Réunion Island, France), CRZF (Port Alfred - Ile de la Possession - Crozet Islands, France), and AIS (Nouvel Amsterdam, TAAF, France). Labels (V) and (H) show the vertical and horizontal components due to translational motion, and (H+T) shows the horizontal component including the tilt effect. The f_{β} values are shown by black arrows. Station locations are shown in Figure 8. Red and blue arrows at 0 mHz show theoretical amplitudes for a flat ocean (Ben-Menahem & Singh, 2000) in vertical and horizontal components respectively.

481 Figure 3a and Figure 10 also show that the transfer functions approaching zero frequency
 482 also approach the above values.

483 **7 Potential applications for ocean infragravity waves**

484 Although tsunami in this frequency range is ocean infragravity waves excited by
 485 an earthquake, ocean infragravity waves are also excited by the other geophysical pro-
 486 cesses. For example, they are excited persistently along shorelines by incident ocean swell
 487 through nonlinear processes, and travel across the ocean with a typical height on the or-
 488 der of 1 cm in pelagic regions (Rawat et al., 2014; Tonegawa et al., 2018). The background
 489 ocean infragravity-wave activities are also key for understanding background seismic wave-
 490 fields know as seismic hum because they are the primary excitation source (Ardhuin, Gualtieri,
 491 & Stutzmann, 2015; Nishida, 2013, 2017; Rhie & Romanowicz, 2004). Observed equipar-
 492 titation between Love and Rayleigh waves (Fukao, Nishida, & Kobayashi, 2010; Nishida,
 493 Kawakatsu, Fukao, & Obara, 2008) suggests topographic coupling between ocean infra-
 494 gravity waves and seismic surface waves. Seismic observations at island broadband sta-
 495 tions could be used to understand the excitation mechanisms because modeling of ocean
 496 infragravity waves requires further research (Ardhuin et al., 2015; Ardhuin, Rawat, &
 497 Aucan, 2014).

498 Our proposed technique for estimating virtual tsunami amplitude is applicable not
 499 only for tsunami but also for random wavefields of the background ocean infragravity
 500 waves. Seismic observations at islands could elucidate ocean infragravity wave activities.
 501 The wave action model WAVEWATCH III has recently been extended from the swell
 502 band to ocean infragravity waves (Ardhuin et al., 2014) and recovers the observed en-
 503 ergy of wave height within 50%. Our method could be used to improve such models.

504 **8 Conclusions**

505 In this study, we consider that an arbitrary tsunami in a flat ocean floor enters a
 506 conical island. The scattering wavefield is evaluated using a semi-analytical method, which
 507 is an extension of the theory of Fujima and Goto (1994). Then, we calculate ground de-
 508 formation due to tsunami loading at the center of the conical island using static Green's
 509 functions with a first-order correction for bathymetry. In this formulation, the ground
 510 motions can be represented by convolution between the transfer functions and the in-
 511 cident tsunami amplitudes at the station. The transfer functions are characterized by

512 a cutoff frequency, f_β , and they approach those given by Ben-Menahem and Singh (2000)
513 for a semi-infinite medium loaded by pressure on the surface without an island. By de-
514 convolving the transfer functions from seismic data, we can infer the incident tsunami
515 wavefield, which can be interpreted as the virtual tsunami amplitude without the island.
516 Thus, we propose a new technique for estimating the virtual tsunami amplitude and prop-
517 agation direction from seismic data using the assumption of a single plane wave.

518 First, we apply this technique to seismic records from Aogashima volcanic island
519 when the Torishima Oki earthquake hit on May 2, 2015. The estimated tsunami ampli-
520 tude is quantitatively consistent with an array observation of pressure gauges close to
521 the island from 1.5 to 20 mHz. The incident angle estimated from the seismic data is
522 also consistent with the ray theoretical value. We also apply this method to seismic data
523 at four broadband stations located on islands in the Indian ocean for the tsunami earth-
524 quake in Mentawai, Indonesia on October 25, 2010. Although the observed frequency
525 range is limited from 0.5 to 2.0 mHz, the incident angles are consistent with ray theo-
526 retical values. This method can therefore complement offshore tsunami observations.

527 Because this technique is formulated for an arbitrary incident wavefield, it could
528 be employed not only for tsunami but also for background ocean infragravity waves, which
529 are excited along shorelines by incident ocean swell through nonlinear processes. Fur-
530 ther research should develop this method in order to elucidate background ocean infra-
531 gravity wave activities using broadband seismic stations located on islands.

A Correction of ground deformation for tilt

Following Segall (2010), we estimate the first order correction of displacements $u_i^{(1)}$ ($i = x, y, z$) for the bathymetry as induced displacement by the first order stress $\sigma_{ij}^{(1)}$ in a cylindrical coordinate (r, θ, z) , given by

$$\sigma_{zz}^{(1)} = 0, \quad (\text{A.1})$$

$$\sigma_{rz}^{(1)} = -\frac{dh}{dr}(\sigma_{zz}^{(0)} - \sigma_{rr}^{(0)}), \quad (\text{A.2})$$

$$\sigma_{\theta z}^{(1)} = -\frac{dh}{dr}\sigma_{r\theta}^{(0)} \quad (\text{A.3})$$

at $z = 0$. Here, the 0th-order terms in Cartesian coordinates satisfy

$$\frac{\partial \sigma_{ij}^{(0)}}{\partial x_j} = 0 \quad (\text{A.4})$$

with boundary conditions given by

$$\sigma_{zz}^{(0)} = -p(x, y), \sigma_{zx}^{(0)} = 0, \sigma_{zy}^{(0)} = 0. \quad (\text{A.5})$$

We note the following relationships:

$$\left. \frac{\partial \sigma_{rz}^{(0)}}{\partial z} \right|_{z=0} = \left. \frac{\partial \sigma_{\theta z}^{(0)}}{\partial z} \right|_{z=0} = \left. \frac{\partial \sigma_{zz}^{(0)}}{\partial z} \right|_{z=0} = 0, \quad (\text{A.6})$$

on the free surface of the island. This result is obtained by representing the stress in terms of the Newtonian potential functions (Love, 1929, section 1.1).

The first order displacement can be calculated by convolution between the Green's function in a semi-infinite medium and $\sigma_{ij}^{(1)}$ on the surface. The corresponding components ($\sigma_{rz}^{(1)}$ and $\sigma_{r\theta}^{(1)}$) can be calculated by convolution between $-p$ and static Green's functions of surface traction for normal traction in a semi-infinite space (Jaeger et al., 2007; Segall, 2010). The Green's functions $g_{xx}^{\sigma z}, g_{xy}^{\sigma z}, g_{yy}^{\sigma z}$ in a Cartesian coordinate system are given by

$$g_{xx}^{\sigma z} = \frac{1}{2\pi} \frac{\mu}{\lambda + \mu} \frac{-x^2 + y^2}{r^4} + \frac{1 + 2\nu}{2} \delta(r), \quad (\text{A.7})$$

$$g_{xy}^{\sigma z} = -\frac{1}{2\pi} \frac{\mu}{\lambda + \mu} \frac{2xy}{r^4}, \quad (\text{A.8})$$

$$g_{yy}^{\sigma z} = \frac{1}{2\pi} \frac{\mu}{\lambda + \mu} \frac{x^2 - y^2}{r^4} + \frac{1 + 2\nu}{2} \delta(r). \quad (\text{A.9})$$

Note that Jaeger et al. (2007) does not include two terms of $\delta(r)$ because they are defined outside the source regions. The two terms can be estimated as the limit of a disk load given by Farrell (1972) as r approaches 0, as shown in the next section. For the convolution between $g_{ij}^{\sigma z}$ and $\sigma_{ij}^{(0)}$, calculation in the wavenumber domain is convenient (Segall,

562 2010). $G_{ij}^{\sigma z}$, which is the Fourier component of $g_{ij}^{\sigma z}$ in the wavenumber domain, is given
 563 by

$$564 \quad G_{xx}^{\sigma z} = \frac{1}{2} \frac{\mu}{\lambda + \mu} \frac{-k_x^2 + k_y^2}{k_x^2 + k_y^2} + \frac{1 + 2\nu}{2} \quad (\text{A.10})$$

$$565 \quad G_{xy}^{\sigma z} = \frac{1}{2} \frac{\mu}{\lambda + \mu} \frac{-2k_x k_y}{k_x^2 + k_y^2} \quad (\text{A.11})$$

$$566 \quad G_{yy}^{\sigma z} = \frac{1}{2} \frac{\mu}{\lambda + \mu} \frac{k_x^2 - k_y^2}{k_x^2 + k_y^2} + \frac{1 + 2\nu}{2} \quad (\text{A.12})$$

567

568 Figure A.1 shows a typical example of induced 0th-order stress $\sigma_{zz}^{(0)} - \sigma_{rr}^{(0)}$ and $\sigma_{r\theta}^{(0)}$,
 569 which is stress induced by the tsunami wavefield with an azimuthal order of 1 ($\zeta_1^{in} =$
 570 1) for Aogashima at 4 mHz. Because $\sigma_{zz}^{(0)} - \sigma_{rr}^{(0)}$ and $\sigma_{r\theta}^{(0)}$ are an order of magnitude smaller
 571 than $\sigma_{zz}^{(0)}$ at the surface, we can neglect the first order stress $\sigma_{ij}^{(1)}$. Consequently, the first
 572 order displacement $u^{(1)}$ is also negligible. Although the first order correction of normal
 573 traction $\sigma_{zz}^{(1)}$ is negligible, those of shear traction, $\sigma_{zx}^{(1)}$ and $\sigma_{zy}^{(1)}$, are significant.

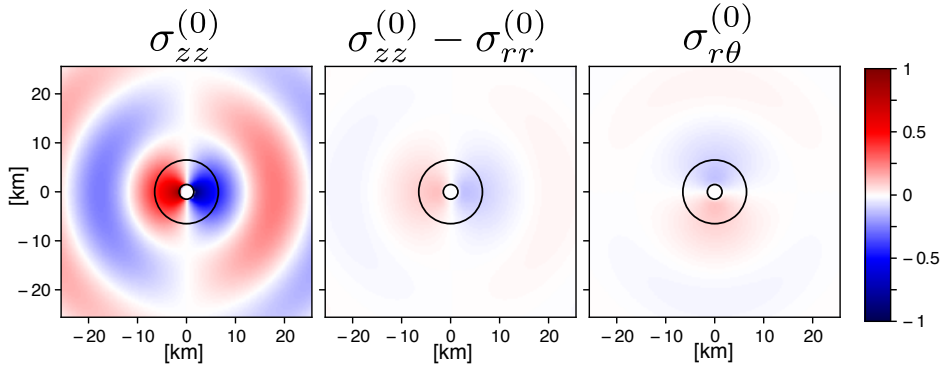


Figure A.1. Stress σ_{zz} is imposed on the surface. σ_{rr} is the induced principle stress on the surface, which is one order of magnitude smaller than the imposed stress. The inner circle shows the radius of the island at sea level, r_0 , and the outer circle shows the radius of the island on the seafloor r_1 .

B Stress components by surface loads on a half-space

Stress components by surface loads on a half-space are given Jaeger et al. (2007)

as

$$\sigma_{xx} = \frac{1}{2\pi} \left[\frac{3x^2z}{r^5} + \frac{(1-2\nu)(y^2+z^2)}{r^3(z+r)} - \frac{(1-2\nu)z}{r^3} - \frac{(1-2\nu)x^2}{r^2(z+r)^2} \right] \quad (\text{B.1})$$

$$\sigma_{xy} = \frac{1}{2\pi} \left[\frac{3xyz}{r^5} - \frac{(1-2\nu)xy(z+2r)}{r^3(z+r)^2} \right] \quad (\text{B.2})$$

$$\sigma_{yy} = \frac{1}{2\pi} \left[\frac{3y^2z}{r^5} + \frac{(1-2\nu)(x^2+z^2)}{r^3(z+r)} - \frac{(1-2\nu)z}{r^3} - \frac{(1-2\nu)y^2}{r^2(z+r)^2} \right]. \quad (\text{B.3})$$

Because the surface values are singular, we derive the simplified form on the surface below.

Let us consider that stress components by a disk load (Love, 1929; Lubarda, 2013) are given by

$$\sigma_{rr} = \frac{p}{2} \begin{cases} 1 + 2\nu, & r < R \\ -(1 - 2\nu)\frac{R^2}{r^2}, & r \geq R \end{cases} \quad (\text{B.4})$$

$$\sigma_{\theta\theta} = \frac{p}{2} \begin{cases} 1 + 2\nu, & r < R \\ (1 - 2\nu)\frac{R^2}{r^2}, & r \geq R \end{cases} \quad (\text{B.5})$$

where R is the radius of the disk and p is the pressure applied uniformly over the disk area. The limits of stress as R approaches 0 have the following forms:

$$\sigma_{xx} = \frac{1}{2\pi} \frac{\mu}{\lambda + \mu} \frac{-x^2 + y^2}{r^4} + \frac{1 + 2\nu}{2} \delta(r) \quad (\text{B.6})$$

$$\sigma_{xy} = -\frac{1}{2\pi} \frac{\mu}{\lambda + \mu} \frac{2xy}{r^4} \quad (\text{B.7})$$

$$\sigma_{yy} = \frac{1}{2\pi} \frac{\mu}{\lambda + \mu} \frac{x^2 - y^2}{r^4} + \frac{1 + 2\nu}{2} \delta(r). \quad (\text{B.8})$$

These representations are also given by the limit of equation B.1 as z approaches 0.

Acknowledgments

We are grateful to a number of people associated with the IRIS, ORFEUS, and F-net data centers for maintaining the networks and making the data readily available. We would like to acknowledge NOAA center for Tsunami Research for the tsunami model of 2010 Mentawai earthquake (<https://nctr.pmel.noaa.gov/indonesia20101025/>). The data analysis was carried out using ObsPy (Krischer et al., 2015). K.N. was supported by JSPS KAKENHI Grant Number JP17H02950 and Y.F. was supported by JSPS KAKENHI Grant Numbers 25247074 and 17K05646. We used data from F-net, which is managed

603 by the National Research Institute for Earth Science and Disaster Prevention (NIED),
604 Japan, and IRIS/IDA Seismic Network (<https://doi.org/10.7914/SN/II>), and GEO-
605 SCOPE (<https://doi.org/10.18715/GEOSCOPE.G>) Institut de Physique du Globe de
606 Paris.

607 **References**

- 608 Aki, K., & Richards, P. G. (1980). *Quantitative Seismology* (Vol. 1). W. H. Free-
 609 man, San Francisco.
- 610 Amante, C., & Eakins, B. W. (2009). *ETOPO1 Global Relief Model con-*
 611 *verted to PanMap layer format* [data set]. PANGAEA. doi: 10.1594/
 612 PANGAEA.769615
- 613 Ardhuin, F., Gualtieri, L., & Stutzmann, E. (2015). How ocean waves rock the
 614 Earth: Two mechanisms explain microseisms with periods 3 to 300 s. *Geophys.*
 615 *Res. Lett.*, *42*(3), 765–772. doi: 10.1002/2014GL062782
- 616 Ardhuin, F., Rawat, A., & Aucan, J. (2014, may). A numerical model for free in-
 617 fragravity waves: Definition and validation at regional and global scales. *Ocean*
 618 *Model.*, *77*, 20–32. doi: 10.1016/j.ocemod.2014.02.006
- 619 Ben-Menahem, A., & Singh, S. J. (2000). *Seismic Waves and Sources* (2nd ed.).
 620 Dover Publications, Incorporated.
- 621 Bernard, E. N., & Meinig, C. (2011, sep). History and future of deep-ocean tsunami
 622 measurements. In *Ocean. mts/ieee kona* (pp. 1–7). IEEE. doi: 10.23919/
 623 OCEANS.2011.6106894
- 624 Farrell, W. E. (1972). Deformation of the Earth by surface loads. *Rev. Geophys.*,
 625 *10*(3), 761. doi: 10.1029/RG010i003p00761
- 626 Fujima, K., & Goto, C. (1994). Characteristics of long waves trapped by conical is-
 627 lands, in japanese. *The Japan Society of Civil Engineers, 1994* (497), 101-110.
 628 doi: 10.2208/jscej.1994.497_101
- 629 Fukao, Y., Nishida, K., & Kobayashi, N. (2010). Seafloor topography, ocean in-
 630 fragravity waves, and background Love and Rayleigh waves. *J. Geophys. Res.*
 631 *Solid Earth*, *115*(4), 1–10. doi: 10.1029/2009JB006678
- 632 Fukao, Y., Sandanbata, O., Sugioka, H., Ito, A., Shiobara, H., Watada, S., & Sa-
 633 take, K. (2018). Mechanism of the 2015 volcanic tsunami earthquake near
 634 Torishima, Japan Mechanism of volcanic tsunami earthquake. *Sci. Adv.*.
- 635 Gica, E., Spillane, M., Titov, V., Chamberlin, C., & Newman, J. (2008). *Develop-*
 636 *ment of the forecast propagation database for NOAA’s Short-Term Inundation*
 637 *Forecast for Tsunamis (SIFT)* (Tech. Rep.).
- 638 Jaeger, J., Cook, N., & Zimmerman, R. (2007). *Fundamentals of rock mechanics*.
 639 Wiley.

- 640 Kanamori, H., Ekström, G., Dziewonski, A., Barker, J. S., & Sipkin, S. A. (1993).
 641 Seismic radiation by magma injection: An anomalous seismic event near
 642 Tori Shima, Japan. *J. Geophys. Res. Solid Earth*, *98*(B4), 6511–6522. doi:
 643 10.1029/92JB02867
- 644 Kimura, T., Tanaka, S., & Saito, T. (2013). Ground tilt changes in Japan caused by
 645 the 2010 Maule, Chile, earthquake tsunami. *Journal of Geophysical Research:
 646 Solid Earth*, *118*(1), 406–415. doi: 10.1029/2012JB009657
- 647 Krischer, L., Megies, T., Barsch, R., Beyreuther, M., Lecocq, T., Caudron, C., &
 648 Wassermann, J. (2015). ObsPy: A bridge for seismology into the scientific
 649 Python ecosystem. *Comput. Sci. Discov.*, *8*(1). doi: 10.1088/1749-4699/8/1/
 650 014003
- 651 Lay, T., Ammon, C. J., Kanamori, H., Yamazaki, Y., Cheung, K. F., & Hutko, A. R.
 652 (2011). The 25 October 2010 Mentawai tsunami earthquake (M w 7.8) and
 653 the tsunami hazard presented by shallow megathrust ruptures. *Geophys. Res.
 654 Lett.*, *38*(6), 2–6. doi: 10.1029/2010GL046552
- 655 Liu, P. L.-F., Cho, Y.-S., Briggs, M. J., Lu, U. K., & Synolakis, C. E. (1995).
 656 Runup of solitary waves on a circular island. *Journal of Fluid Mechanics*,
 657 *302*(10), 259–285. doi: 10.1017/S0022112095004095
- 658 Longuet-Higgins, M. S. (1967). On the trapping of wave energy round islands. *J.
 659 Fluid Mech.*, *29*(04), 781–821. doi: 10.1017/S0022112067001181
- 660 Love, A. E. H. (1929). The Stress Produced in a Semi-Infinite Solid by Pressure
 661 on Part of the Boundary. *Philos. Trans. R. Soc. A Math. Phys. Eng. Sci.*,
 662 *228*(659-669), 377–420. doi: 10.1098/rsta.1929.0009
- 663 Lubarda, V. A. (2013). Circular loads on the surface of a half-space: Displace-
 664 ment and stress discontinuities under the load. *Int. J. Solids Struct.*, *50*(1), 1–
 665 14. doi: 10.1016/j.ijsolstr.2012.08.029
- 666 Moré, J. J., Sorensen, D. C., Hillstrom, K. E., & Garbow, B. S. (1984). *The MIN-
 667 PACK Project, in Sources and Development of Mathematical Software*. Upper
 668 Saddle River, NJ, USA: Prentice-Hall, Inc.
- 669 Nawa, K., Suda, N., Satake, K., Fujii, Y., Sato, T., Doi, K., ... Shibuya, K. (2007).
 670 Loading and gravitational effects of the 2004 Indian Ocean tsunami at Syowa
 671 Station, Antarctica. *Bull. Seismol. Soc. Am.*, *97*(1A), S271–S278. doi:
 672 10.1785/0120050625

- 673 Nishida, K. (2013). Earth's Background Free Oscillations. *Annu. Rev. Earth Planet.*
674 *Sci.*, *41*(1), 719–740. doi: 10.1146/annurev-earth-050212-124020
- 675 Nishida, K. (2017). Ambient seismic wave field. *Proc. Japan Acad. Ser. B*, *93*(7),
676 423–448. doi: 10.2183/pjab.93.026
- 677 Nishida, K., Kawakatsu, H., Fukao, Y., & Obara, K. (2008, aug). Background Love
678 and Rayleigh waves simultaneously generated at the Pacific Ocean floors. *Geo-*
679 *phys. Res. Lett.*, *35*(16), L16307. doi: 10.1029/2008GL034753
- 680 Okada, Y., Kasahara, K., Hori, S., Obara, K., Sekiguchi, S., Fujiwara, H., & Ya-
681 mamoto, A. (2004). Recent progress of seismic observation networks in Japan
682 Hi-net, F-net, K-NET and KiK-net. *Earth, Planets Sp.*, *56*(8), xv–xxviii. doi:
683 10.1186/BF03353076
- 684 Radhakrishnan, K., & Hindmarsh, A. C. (1993, dec). *Description and use of*
685 *LSODE, the Livermore Solver for Ordinary Differential Equations* (Tech.
686 Rep.). Livermore, CA: Lawrence Livermore National Laboratory (LLNL).
687 doi: 10.2172/15013302
- 688 Rawat, A., Arduin, F., Ballu, V., Crawford, W., Corela, C., & Aucan, J. (2014,
689 nov). Infragravity waves across the oceans. *Geophys. Res. Lett.*, *41*(22),
690 7957–7963. doi: 10.1002/2014GL061604
- 691 Rawlinson, N. (2005). *FMST: Fast Marching Surface Tomography package Research*
692 (Tech. Rep.). Aust. Natl. Univ.
- 693 Rawlinson, N., & Sambridge, M. (2005). The fast marching method: An effective
694 tool for tomographic imaging and tracking multiple phases in complex layered
695 media. *Explor. Geophys.*, *36*(4), 341–350. doi: 10.1071/EG05341
- 696 Rhie, J., & Romanowicz, B. (2004, sep). Excitation of Earth's continuous free oscil-
697 lations by atmosphereoceanseafloor coupling. *Nature*, *431*(7008), 552–556. doi:
698 10.1038/nature02942
- 699 Rodgers, P. W. (1968). The response of the horizontal pendulum seismometer to
700 Rayleigh and Love waves, tilt, and free oscillations of the earth. *Bull. Seismol.*
701 *Soc. Am.*, *58*(5), 1385–1406.
- 702 Sandanbata, O., Watada, S., Satake, K., Fukao, Y., Sugioka, H., Ito, A., & Shiobara,
703 H. (2017). Ray Tracing for Dispersive Tsunamis and Source Amplitude Es-
704 timation Based on Green's Law: Application to the 2015 Volcanic Tsunami
705 Earthquake Near Torishima, South of Japan. *Pure Appl. Geophys.*. doi:

- 706 10.1007/s00024-017-1746-0
- 707 Satake, K. (2015). Tsunamis. In *Treatise geophys.* (pp. 477–504). Elsevier. doi: 10
- 708 .1016/B978-0-444-53802-4.00086-5
- 709 Satake, K., Fujii, Y., Harada, T., & Namegaya, Y. (2013). Time and space dis-
- 710 tribution of coseismic slip of the 2011 Tohoku earthquake as inferred from
- 711 Tsunami waveform data. *Bull. Seismol. Soc. Am.*, *103*(2 B), 1473–1492. doi:
- 712 10.1785/0120120122
- 713 Satake, K., & Kanamori, H. (1991). Abnormal tsunamis caused by the June 13,
- 714 1984, Torishima, Japan, earthquake. *J. Geophys. Res. Solid Earth*, *96*(B12),
- 715 19933–19939. doi: 10.1029/91JB01903
- 716 Satake, K., Nishimura, Y., Putra, P. S., Gusman, A. R., Sunendar, H., Fujii, Y., ...
- 717 Yulianto, E. (2013). Tsunami Source of the 2010 Mentawai, Indonesia Earth-
- 718 quake Inferred from Tsunami Field Survey and Waveform Modeling. *Pure*
- 719 *Appl. Geophys.*, *170*(9-10), 1567–1582. doi: 10.1007/s00024-012-0536-y
- 720 Segall, P. (2010). *Earthquake and Volcano Deformation*. Princeton University Press.
- 721 Sorrells, G. G., & Goforth, T. T. (1973). Low-Frequency Earth Motion Gener-
- 722 ated By Slowly Propagating Partially Organized Pressure Fields. *Bull. Seis-*
- 723 *mol. Soc. Am.*, *63*(5), 1583–1601.
- 724 Tonegawa, T., Fukao, Y., Shiobara, H., Sugioka, H., Ito, A., & Yamashita, M.
- 725 (2018). Excitation Location and Seasonal Variation of Transoceanic Infra-
- 726 gravity Waves Observed at an Absolute Pressure Gauge Array. *J. Geophys.*
- 727 *Res. Ocean.*, 40–52. doi: 10.1002/2017JC013488
- 728 Wielandt, E., & Forbriger, T. (1999). Near-field seismic displacement and tilt asso-
- 729 ciated with the explosive activity of Stromboli. *Ann. Geophys.*, *42*(3), 407–416.
- 730 doi: 10.4401/ag-3723
- 731 Williams, C. A., & Wadge, G. (2000). An accurate and efficient method for includ-
- 732 ing the effects of topography in three-dimensional elastic models of ground
- 733 deformation with applications to radar interferometry. *J. Geophys. Res.*,
- 734 *105*(B4), 8103–8120. doi: 10.1029/1999JB900307
- 735 Yuan, X., Kind, R., & Pedersen, H. (2005). Seismic monitoring of the Indian Ocean
- 736 tsunami. *Geophys. Res. Lett.*, *32*(15), L15308. doi: 10.1029/2005GL023464